Simulated ALMA observations of collapsing low-mass dense cores

F. Levrier [1] **B. Commerçon** [1,3] **A. J. Maury** [2]

Th. Henning [3] **R. Launhardt** [3] **C. Dullemond** [4]

1 : LERMA/LRA - UMR 8112 - Ecole Normale Supérieure, 24 rue Lhomond, 75231 Paris CEDEX 05, France
2 : ESO, Karl Schwarzschild Straße 2, 85748, Garching bei München, Germany
3 : Max Planck Institut für Astronomie, Königsthul 17, 69117 Heidelberg, Germany
4 : Zentrum für Astronomie der Universität Heidelberg, Institut für Theoretische Astrophysik, Albert-Ueberle-Straße 2, 69120 Heidelberg, Germany

Abstract

Although predicted by theoretical models, the existence of first hydrostatic cores (FHSC) has yet to be convincingly demonstrated by (sub)millimeter observations, and the multiplicity at this early stage of the star formation process is poorly constrained.

We present a possible identification strategy for FHSC candidates and make predictions of ALMA dust continuum emission maps from these objects. This is done by post-processing three state-of-the-art radiation-magneto-hydrodynamic 3D adaptive mesh refinement calculations of first hydrostatic core models performed with the RAMSES code. We compute the dust thermal continuum emission with the 3D radiative transfer code RADMC-3D, then produce synthetic ALMA observations using the simulator included in the GILDAS software package.

We analyze the results given by the different bands and array configurations and identify which combinations of the two represent our best chance of solving the fragmentation issue in these objects. We thus demonstrate how ALMA will help in identifying the physical processes occurring within collapsing dense cores : If the magnetic field is playing a role, the emission pattern will show evidence of a pseudo-disk and even of a magnetically driven outflow, which pure hydrodynamical calculations cannot reproduce.

An actively pursued extension of this work is the inclusion of chemical processes in the collapsing core and the consequent search for line emission observational diagnostics.

1 RMHD models of core collapse

The models of protostellar core collapse are built using the adaptive-mesh refinement code RAMSES [3], which integrates the equations of ideal MHD [4,5] and the equations of radiation hydrodynamics under the gray flux-limited diffusion approximation [6].

A 1 solar mass sphere of gas with initial radius 3300 AU and uniform density and temperature is put into solid body rotation [7]. Initially defined on a 64^3 grid, ten possible levels of refinement provide the models with an effective resolution of 0.2 AU.

Three models are presented, corresponding to three levels of magnetization expressed in terms of the mass-to-flux to critical mass-to-flux ratio μ. They are synchronized at a time t_0 when maximum grid refinement is attained, roughly when the FHSC is formed.

The simulations are stopped after a time Δt, when temperatures reach some 1200 K, for which dust begins to evaporate, dramatically lowering the opacities [8] - which are taken from [9] - and opening the way to the second collapse. This FHSC lifetime depends strongly on the magnetization level [1,10] because accretion increases with magnetic braking [7,11].

- **Initial density** $\rho_0 = 3.97\ 10^{-18}\ \mathrm{g.cm^{-3}}$
- **Initial temperature** $T_0 = 11\ \mathrm{K}$
- **Initial magnetic field geometry** $\mathbf{B}_0 = B_0 \mathbf{e}_z$
- **Initial energy ratio** $E_{\mathrm{rot}}/E_{\mathrm{grav}} = 0.045$
- **Ratio of specific heats** $\gamma = 5/3$
- **Perfect thermal coupling** $T_{\mathrm{dust}} = T_{\mathrm{gas}}$
- **No scattering**

Strong magnetization	*Intermediate magnetization*	*Quasi-hydro case*
$\mu = 2$	$\mu = 10$	$\mu = 200$
$t_0 = 50.4$ kyr	$t_0 = 35.7$ kyr	$t_0 = 35.4$ kyr
$\Delta t = 1.2$ kyr	$\Delta t = 2.94$ kyr	$\Delta t > 4.4$ kyr

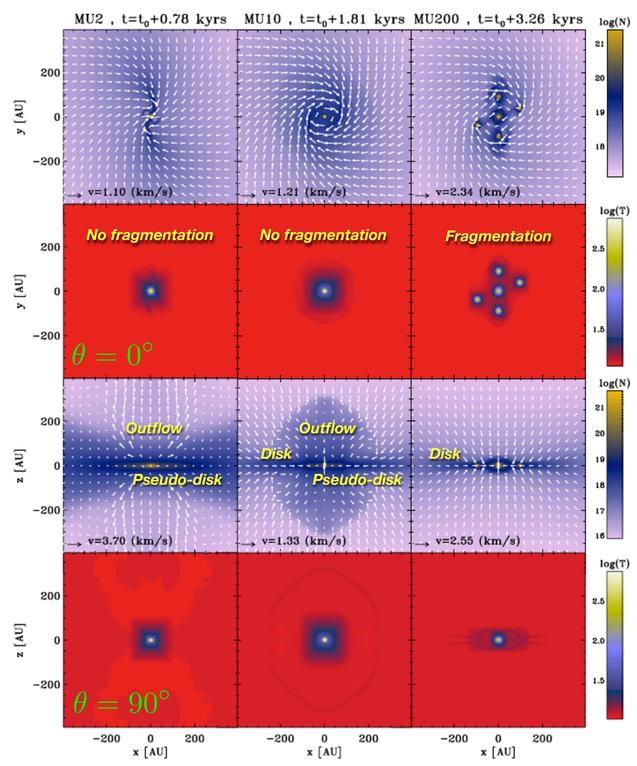

Fig. 1 : Column density and temperature maps in the *xOy*-plane (two upper rows) and *xOz*-plane (two lower rows) for the MU2 (left), MU10 (middle) and MU200 (right) models. Scales are logarithmic, and column density is given in $\mathrm{cm^{-2}}$. Figure adapted from [1].

2 Identification of FHSC candidates from SED

The RMHD models are post-processed using the RADMC-3D code, developed by C. Dullemond [12], which, among other features, allows to build images and spectral energy distributions (SED) of dust thermal emission.

The SED presented here are computed assuming a distance of 150 pc and a 20" aperture, which amounts to integrating over a 3000 AU by 3000 AU area. Models are observed at three different inclination angles, from a pole-on view to an edge-on view.

The strongly magnetized (MU2) and quasi-hydro (MU200) models show a clear and similar evolutionary sequence, with a significant amount of flux emitted in the later stages between 20μm and 100 μm, when viewing models close to pole-on. This is in contradiction to what was found in previous studies, which assumed spherical symmetry [13]. In that case, envelopes are not thick enough to fully reprocess the central object's radiation. The edge-on view in our models shows no such flux enhancement, which agrees with this geometrical interpretation.

The SED in the intermediately magnetized model (MU10) shows no evolution, because the combination of a disk, a pseudo-disk and a dense outflow leads to a complete reprocessing of the FHSC's radiation before it is able to escape towards the observer.

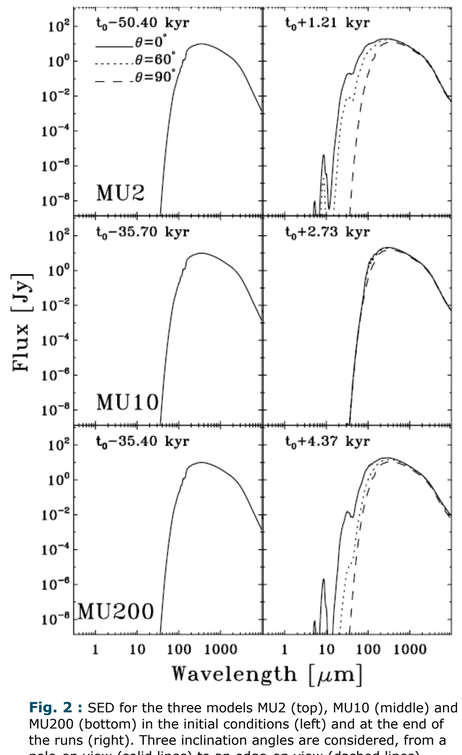

Fig. 2 : SED for the three models MU2 (top), MU10 (middle) and MU200 (bottom) in the initial conditions (left) and at the end of the runs (right). Three inclination angles are considered, from a pole-on view (solid lines) to an edge-on view (dashed lines). Figure taken from [1].

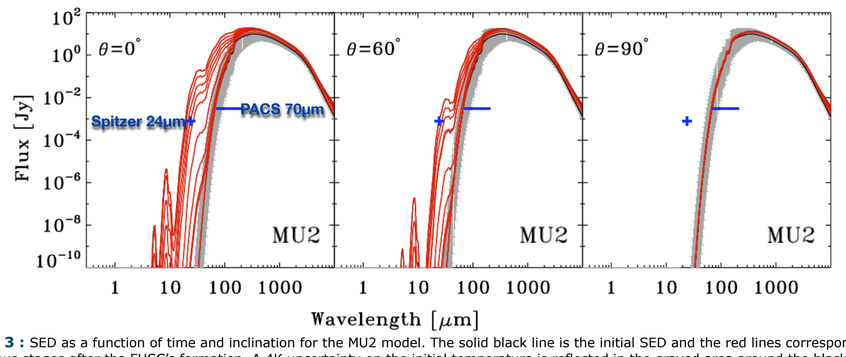

Fig. 3 : SED as a function of time and inclination for the MU2 model. The solid black line is the initial SED and the red lines correspond to various stages after the FHSC's formation. A 4K uncertainty on the initial temperature is reflected in the grayed area around the black line. The blue cross is the 3σ/24s sensitivity with SPITZER at 24μm [14], and the blue line is the 5σ/1hr sensitivity with Herschel / PACS at 70 μm [15]. Figure adapted from [1].

3 Simulated ALMA observations of the dust thermal continuum

Although point-source detections below 100 μm combined with non detections below 10 μm may help identify FHSC candidates, high-resolution interferometric observations are necessary to distinguish between a non-magnetized and a strongly magnetized scenario.

We used the ALMA simulator included in the GILDAS software package [16,17] to predict what may be observed by ALMA when targeting FHSC candidates. To this end, we produced dust emission maps with RADMC-3D in bands 3, 4, 6, 7 and 9, and used these as input brightness distributions for the ALMA simulator. We considered four typical configurations of the full array, but did not include the ALMA Compact Array (ACA). Simulations were performed for the three magnetization levels and four inclination angles.

To distinguish between the MU2 and MU200 models, it is necessary to resolve the fragmentation scale of a few AU. Of the four configurations considered here, C=15 and C=20 provide the best sampling of these spatial scales.

They however have a larger central hole in Fourier space, which means that they miss more of the large-scale flux than C=5 and C=10. This flux loss becomes more important at higher frequencies, because a given baseline then corresponds to smaller scales in the observed brightness distribution.

Overall, it appears that, for FHSC candidates at 150 pc, observing below 150 GHz with a configuration providing best sampling around 500 m to 1 km baselines provides a limited flux loss and the ability to resolve the fragmentation scale, thus suggesting an observing strategy for forthcoming ALMA proposals.

Emission maps with these parameters indeed show a clear distinction between the magnetized models (MU2 and MU10) and the quasi-hydro case MU200, and the different features from the RMHD models (disk, pseudo-disk, outflow) appear quite clearly and above the noise level in the simulated dust emission maps.

The simulated maps presented here assume 18 minute runs of observation, so that many FHSC candidates may be observed in a single observing proposal.

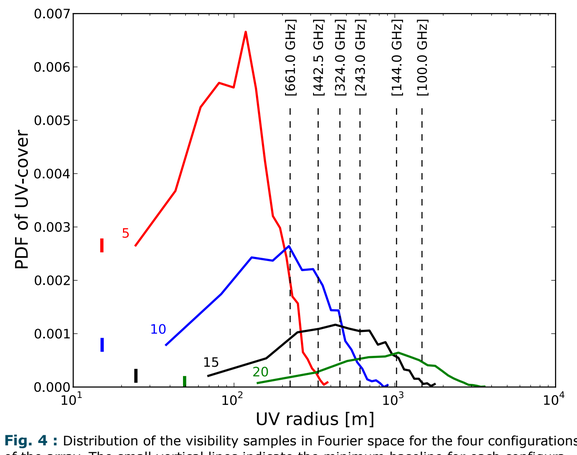

Fig. 4 : Distribution of the visibility samples in Fourier space for the four configurations of the array. The small vertical lines indicate the minimum baseline for each configuration, and the dashed lines indicate, for each frequency, the characteristic baselines corresponding to a physical scale of 10 AU, comparable to the fragmentation scale. Figure taken from [2].

B	ν_0 [GHz]	$\Delta\nu_0$ [GHz]	FoV ["]	Early Science
3	100	32	63	Yes
4	144	38	44	No
6	243	64	26	Yes
7	324	98	19	Yes
8	442.5	115	14	No
9	661	118	9.5	Yes

Tab. 1 : Characteristics of the ALMA bands used (*B*). Listed are the central frequency, full bandwidth, field-of-view at the band center, and availability in the Early Science phase. Table taken from [2].

C	b_{min} [m]	b_{maj} [m]	θ_3 ["]	θ_9 ["]
5	15	390	2.47×2.12	0.37×0.32
10	20	924	1.07×0.99	0.16×0.15
15	25	1814	0.48×0.43	0.07×0.06
20	49	3699	0.24×0.22	0.04×0.03

Tab. 2 : Characteristics of the full ALMA configurations used (*C*). Listed are the minimum and maximum baselines and the synthesized beamwidths (FWHM) in bands 3 and 9. Table taken from [2].

Fig. 7 : Simulated brightness distribution map for an observation with a C=20 full ALMA array at 144 GHz combined with single-dish measurement of the total flux, including 0.6 mas pointing errors on all antennas, realistic thermal noise and uncorrected atmospheric phase noise with a 45º rms phase difference on 300 m baselines. Contours correspond to the 3σ sensitivity limit in this band and these conditions, which is σ=17.41 μJy. Figure adapted from [2].

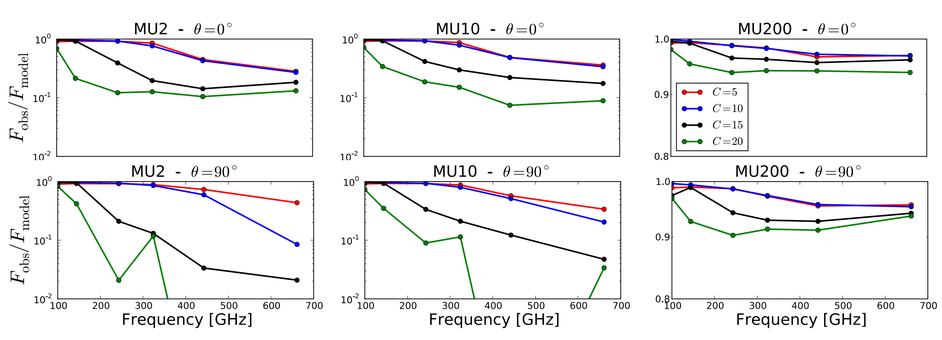

Fig. 5 : Ratio of the observed to model flux as a function of frequency, for the three different magnetization levels (magnetic field decreasing from left to right), four array configurations, and two of the four inclination angles (from pole-on view in the top row to edge-on view in the bottom row). Figure adapted from [2].

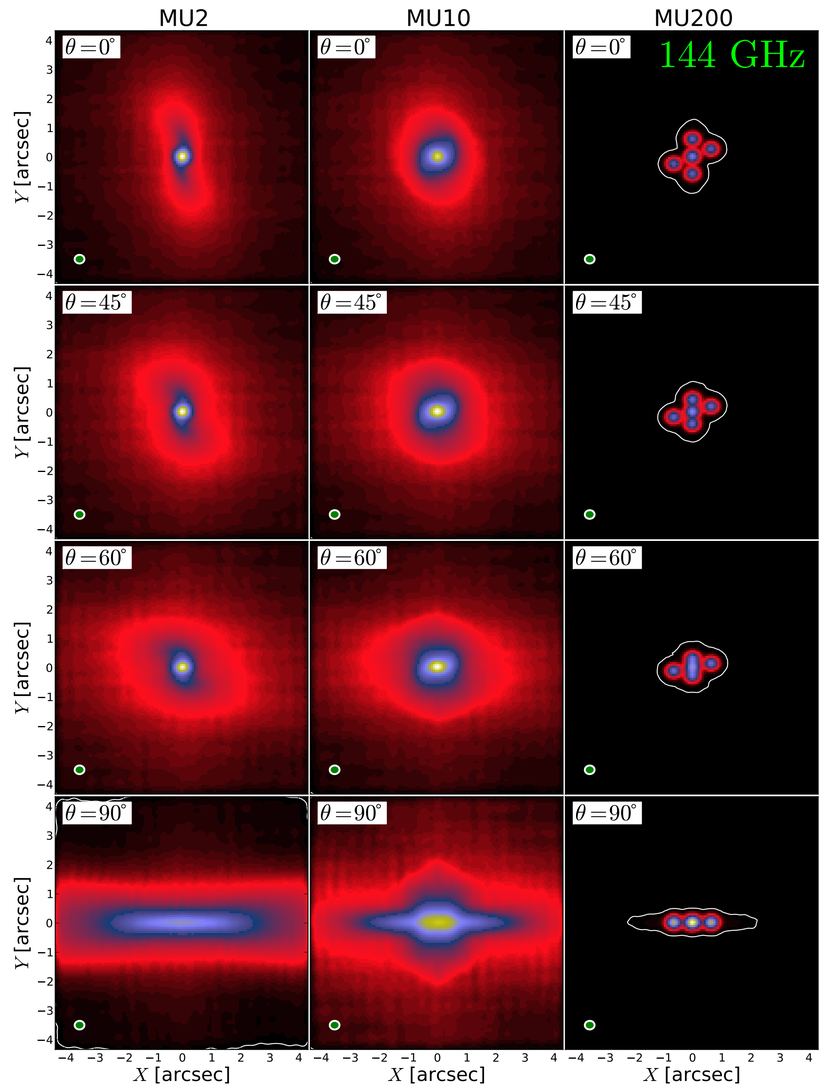

Fig. 6 : Simulated ALMA dust emission maps at 144 GHz in configuration *C*=15 for the MU2 (left), MU10 (middle) and MU200 (right) models. Four inclination angles are presented, from pole-on view (top) to edge-on view (bottom). Color scales are in Jy/beam and contours show the 3σ sensitivity limit in this band, with σ=16.05 μJy. The synthesized beam is shown in the bottom left corner of each plot. Figure adapted from [2].

4 Perspectives

The lifetime of FHSC is quite short [18,10], and as soon as central temperatures allow dust evaporation (1200 K) then H_2 dissociation (2000 K), the core undergoes a second collapse leading up to the formation of the second hydrostatic core (SHSC), i.e. the Class 0 protostar.

Our work is currently limited to thermal dust continuum emission before this stage, and as such cannot be expected to provide clues towards distinguishing FHSC and SHSC. In any case, almost all thermal dust radiation emitted by either type of object would be reprocessed by their dense envelopes, so different approaches are required.

One such approach would be to focus on chemical properties, which are indicative of the local thermal history in these objects [19]. For instance, elements such as C and Si are released into the gas phase when dust evaporates, thereby altering chemical pathways and abundances [8,20]. This chemical approach would be especially useful when targeting the outflow : the low-velocity outflow from a FHSC should show signs of low temperature chemistry, while the high-velocity outflow from the SHSC should show signs of high temperature chemistry.

These effects are being investigated upon by U. Hincelin, V. Wakelam, A. Dutrey, S. Guilloteau and F. Hersant (LAB), in collaboration with us, using the chemical code Nautilus [21] on our RMHD models. This is done by introducing tracer particles in the RAMSES simulations, and using their density and temperature history to compute their chemical evolution [22], ignoring any feedback effects of chemistry on dynamics [23], chemical diffusion, or for the moment chemistry at temperatures above 300 K [24].

We are currently working on interfacing the outputs of Nautilus with RADMC-3D's line radiative transfer capabilities to build simulated spectro-imagery simulations in various tracers (CO, $C^{17}O$, $C^{18}O$,H_2D^+,...). This should provide further clues for observational diagnostics towards the detection of FHSC.

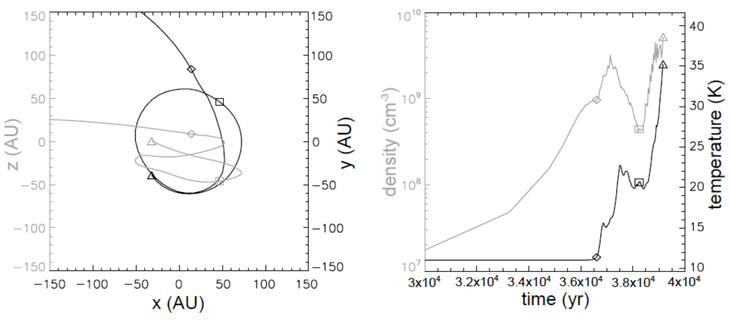

Fig. 8 : On the left is an example trajectory of a tracer particle injected in a collapsing core RMHD model. Coordinates in the equatorial plane *xOz* are given in grey and those in a meridian plane *xOy* in black. Plotted on the right are the density (grey) and temperature (black) time evolutions of that tracer particle as it falls towards the central core. Triangles, squares and lozenges on both plots indicate which position, density and temperatures are reached at these times. Figure courtesy of U. Hincelin [22].

Fig. 9 : Gas-phase abundance of CO with respect to H atoms, at the end of the simulation for the MU10 model (some 38 kyr). Presented are projections of the particles' positions on the *xOy* (left) and *xOz* (right) planes, taking into account only particles located within 50 AU of these planes. Due to the limited number of particles used (10^6), and their tendency to cluster along flow lines, these are quite visible. The outflow is also very much apparent in the meridian plane *xOz*. Figure courtesy of U. Hincelin [22].

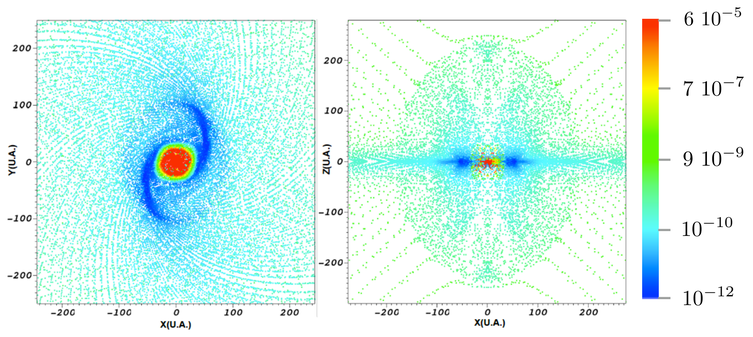

References

[1] Commerçon, B., Launhardt, R., Dullemond, C., Henning, Th., 2012, A&A, 545, A98
[2] Commerçon, B., Levrier, F., Maury, A.J., Launhardt, Henning, Th., 2012, A&A, *in press*
[3] Teyssier, R., 2002, A&A, 385, 337
[4] Fromang, S., Hennebelle, P., Teyssier, R., 2006, A&A, 457, 371
[5] Teyssier, R., Fromang, S., Dormy, E., 2006, J. Comput. Phys., 218, 44
[6] Commerçon, B.,Teyssier, R., Audit, E., Hennebelle, P., Chabrier, G., 2011, A&A, 529, A35
[7] Commerçon, B., Hennebelle, P., Audit, E., Chabrier, G., Teyssier, R., 2010, A&A, 510, L3
[8] Lenzuni, P., Gail, H.-P., Henning, Th., 1995, ApJ, 447, 848
[9] Semenov, D., Henning, Th., Helling, C., Ilgner, M., Sedlmayr, E., 2003, A&A, 410, 611
[10] Tomida, K., Machida, M.N., Saigo, K., Tomisaka, K., Matsumoto, T., 2010, ApJ, 725, L239
[11] Joos, M., Hennebelle, P., Ciardi, A., 2012, A&A, 543, A128
[12] Dullemond, C. http://www.ita.uni-heidelberg.de/~dullemond/software/radmc-3d/
[13] Omukai, K., 2007, PASJ, 59, 589
[14] Evans, II, N.J., Allen, L.E., Blake, G.A., *et al.*, 2003, PASP, 115, 965
[15] Poglitsch, A., Waelkens, C., Geis, N., *et al.*, 2010, A&A, 518, L2
[16] http://iram.fr/IRAMFR/GILDAS
[17] Pety, J., Gueth, F., Guilloteau, S., 2001, ALMA Memo 398
[18] Masunaga, H., Inutsuka, S.-I., 2000, ApJ, 531, 350
[19] Kim, H.J., Evans, II, N.J., Dunham, M.M., *et al.*, 2011, ApJ, 729, 84
[20] Albertsson, T., Semenov, D, Henning, Th., ApJ, *submitted, arXiv:1110.2644*
[21] Hersant, F., Wakelam, V., Dutrey, A., Guilloteau, S., Herbst, E., 2009, A&A, 493, L49
[22] Hincelin, U., PhD Thesis, Université Bordeaux 1, 2012
[23] Dedes, C., Herpin, F., Chavarria, L., *et al.*, 2011, in IAU Symposium 280, 149
[24] Harada N., Herbst, E., Wakelam, V., 2010, ApJ, 72, 1570